IL NUOVO CIMENTO **40 C** (2017) 97
DOI 10.1393/ncc/i2017-17097-2

COMMUNICATIONS: SIF Congress 2016

Dosimetry by ^{90}Y internal pair production PET imaging after liver radioembolization: How well can we quantify the absorbed dose to lesions?

M. D'ARIENZO

ENEA, National Institute of Ionizing Radiation Metrology - Via Anguillarese 301, 00123 Rome, Italy

received 3 March 2017

Summary. — Radioembolization is a catheter-based liver-directed therapy indicated mainly in a palliative setting for primary and secondary hepatic malignancies. It involves the administration of ^{90}Y-loaded microspheres in the arterial vasculature of the liver by use of percutaneous transarterial techniques. Previous studies showed that the decay of ^{90}Y has a minor branch to the 0^+ first excited state of ^{90}Zr at 1.76 MeV, that is followed by a β^+/β^- emission. In recent years, a number of authors have used the small positronic emission of ^{90}Y, $(3.186 \pm 0.047) \cdot 10^{-5}$, to obtain high-resolution positron emission tomography (PET) images of ^{90}Y biodistribution after liver radioembolization. At present, it is generally accepted that the possibility of detecting β^+ emissions from ^{90}Y by PET scanners may pave the way for an accurate patient-specific dosimetry. The present paper has a twofold purpose. Firstly, a brief overview of imaging modalities currently used to assess microsphere biodistribution after liver radioembolization is presented. Secondly, the paper focuses on ^{90}Y-PET dosimetry. A benchmark between a number of dosimetric approaches for accurate dosimetry after liver radioembolization with ^{90}Y-PET dosimetry is presented.

1. – Introduction

Therapy with ^{90}Y-microspheres is a widely used treatment modality in the management of patients with primary and metastatic liver cancer. This therapeutic option is also known as *selective internal radiation therapy* (SIRT). SIRT is performed by injecting ^{90}Y microspheres directly into the hepatic artery. In fact, the blood supply of liver lesions is mainly derived from this artery, whereas normal liver tissue receives about 80% of its blood supply from the portal vein. By infusing millions of radioactive beads (^{90}Y resin or glass microspheres) into the arterial blood supply of the liver a high radiation dose can be delivered selectively into the tumour while sparing normal liver tissue that surrounds the tumour compartments.The major advantage of SIRT is that the high selectivity of

the procedure has the potential to deliver absorbed doses up to 40 times higher than conventional radiotherapy, while sparing healthy tissue. Furthermore, the therapeutic ratio with SIRT, compared to external beam radiotherapy, is also significantly improved and the tumour-absorbed doses resulting from SIRT treatments are typically 4 to 6 times higher than those absorbed by the healthy liver tissue. Namely, the delivery of typically recommended doses of ^{90}Y microspheres leads to average absorbed doses greater than 150 Gy to tumour areas, while average doses received by healthy liver parenchyma are of the order of 20–25 Gy [1-3].

After a local anaesthetic is administered to the patient, a small incision (usually into the femoral artery near the groin) is made by the interventional radiologist. A catheter is then guided through the artery into the liver and ^{90}Y-laden beads are administered. The whole procedure may take around 60–90 minutes. After the procedure is completed, patients may be sent to have a scan to check the level of radioactivity of the ^{90}Y microspheres in the liver. Patients will be monitored for a few hours after the procedure and most patients will be discharged within 24 hours.

^{90}Y is produced by bombardment of ^{89}Y with neutrons in nuclear reactors. It has a physical half-life of 64.2 hours (2.67 days), and it decays to stable ^{90}Zr. ^{90}Y emits pure high-energy beta rays (maximum and mean energy 2.27 MeV and 0.9367 MeV, respectively) with an average penetration range of 2.5 mm and a maximum range of 11 mm in tissue. As a rule of thumb, one GBq (27 mCi) of ^{90}Y delivered in 1 kg of tissue provides a total absorbed radiation dose of 50 Gy. In therapeutic use in which the isotope decays to infinity, 94% of the radiation is delivered in 11 days.

At present, there are two clinically available microsphere devices in which ^{90}Y is incorporated: one with microspheres made of glass (TheraSphere; MDS Nordion, Ottawa, Ontario, Canada) and the other with microspheres made of resin (SIR-Spheres; Sirtex Medical, Sydney, Australia). The characteristics of the two devices are reported in table I. The resin microsphere device consists of biocompatible ^{90}Y-bearing microspheres with diameters of 20–40 μm. Once administered, the spheres remain in the liver as a permanent implant. The device is approved for the treatment of unresectable liver metastases from primary colorectal cancer and is used with adjuvant chemotherapy with floxuridine administered via the hepatic artery. Glass microsphere consists of insoluble glass microspheres where ^{90}Y is an integral constituent of the glass. The mean sphere diameter ranges from 20 to 40 μm, approximately. Each milligram contains between 22,000 and 73,000 microspheres.

^{90}Y PET imaging has received much attention in the last few years. At present, it is generally accepted that the possibility of detecting β^+ emissions from ^{90}Y by PET scanners may pave the way for an accurate patient-specific dosimetry. Reliable dose evaluation has become a central issue in molecular radiotherapy as side effects and treatment outcome are related to absorbed doses. As a matter of fact, the last few years have witnessed a huge growth in dosimetric studies following radioembolization with ^{90}Y microspheres. However, there is still much controversy surrounding the most accurate dosimetric approach for the assessment of the absorbed dose.

The present paper is structured as follows. Section **2** provides an overview of imaging modalities currently used to assess microsphere biodistribution after liver radioembolization. In particular ^{99m}Tc SPECT imaging, ^{90}Y bremsstrahlung imaging and ^{90}Y PET imaging will be described (subsects. **2**˙1, **2**˙2 and **2**˙2, respectively). The second section is dedicated to ^{90}Y-PET dosimetry. The major outcomes of a phantom study aimed to benchmark different dosimetric approaches will be presented. Subsections **3**˙1 through **3**˙5 will be dedicated to a brief overview of the computational approaches used

TABLE I. – *Comparison of the two ^{90}Y microsphere devices.*

Characteristics	**Glass microsphere**	**Resin microsphere**
Trade name	TheraSphere	SIR-Sphere
Diameter	$(32 \pm 10)\,\mu$m	$(22 \pm 10)\,\mu$m
Company	Nordion, Canada	Sirtex, Australia
Microspheres per administered activity	1.2–8 million	40–80 million
Specific activity (Bq/sphere)	2500	50
Specific gravity	3.6 g/dL	1.6 g/dL
Material	Glass (yttrium in matrix)	Resin (bound yttrium)
Solution used for suspension of microspheres	Normal saline	Sterile water
Maximal prescribed activity	20	3
Activity available (GBq)	3, 5, 7, 10, 15, 20	3
Embolic effect	Mild	Moderate
Splitting one vial for two or more patients	Not possible	Possible
Relative embolic potential	Higher	Lower

in the experimental activity. Results and discussions will be presented in sect. **4**, while sect. **5** will be dedicated to the conclusions.

2. – Imaging of ^{90}Y microsphere

The role of imaging in radioembolization with ^{90}Y microspheres is fundamental both in patient selection and the assessment of microsphere delivery after the treatment. Further, as described in the following paragraphs, images acquired prior and after the treatment can be used to perform patient-specific dosimetry. In particular, dosimetric studies can be performed *a priori* using pre-treatment ^{99m}Tc images or *a posteriori* on ^{90}Y bremstrahlung images and ^{90}Y-PET/CT after microsphere administration.

2˙1. *^{99m}Tc SPECT imaging.* – Generally, for any selected candidate for radioembolization a pre-treatment angiographic evaluation combined with ^{99m}Tc-macroaggregated albumin (MAA) [4] are required in order to assess the vascular anatomy of the liver. ^{99m}Tc-MAA particle size ranges from 10 to 50 μm (average particle size 35 μm), thus being comparable to resin microspheres. The underlying assumption is that ^{99m}Tc-MAA biodistribution simulates expected microsphere delivery during ^{90}Y radioembolization. It is worth noting that to date correlation between ^{99m}Tc-MAA and ^{90}Y has not reached consensus in the literature, with some paper suggesting an almost perfect agreement [5] and other disagreeement [6].

During SIRT therapy possible extrahepatic shunting leading to potentially high radiation dose to the lungs and to the gastrointestinal tract may represent an absolute contraindication to the treatment. Therefore prophylactic embolization of all extrahepatic vessels, including gastroduodenal artery and right gastric artery is recommended to exclude extrahepatic deposition of microspheres [7].

In particular, arteriography is essential to identify the hepatic arterial supply from the celiac and the superior mesenteric artery, and represents a fundamental procedure to prevent gastrointestinal complications. During selective catheterisation, branches of the hepatic artery, such as the gastroduodenal artery and the right gastric artery, are coil embolised to prevent reflux of ^{90}Y at the gastric and duodenal levels. After this procedure, usually 150 to 300 MBq of ^{99m}Tc-MAA are administered through the catheter

to evaluate possible arteriovenous shunt of the hepatic arterial system to the pulmonary arterial system and/or gastrointestinal venous system. This procedure permits evaluation of possible undesired directions of the ^{90}Y microspheres, which have approximately the same dimensions as the marked albumin particles.

Scintigraphic imaging is typically performed within 1h following ^{99m}Tc-MAA administration on a gamma camera equipped with low-energy high-resolution collimators. It is recommended that the scintigraphic ^{99m}Tc-MAA imaging be performed as soon as possible after radiopharmaceutical administration because free ^{99m}Tc can enter the system circulation and fix itself in the gastric mucosa. The amount of free ^{99m}Tc is usually variable and unpredictable. Therefore, this extrahepatic activity cannot be distinguished from deposition coming from aberrant extrahepatic arteries. In order to overcome this drawback, it is generally recommended to administer perchlorate (Irenate) before the catheterization which completely blocks the uptake of free ^{99m}Tc in the gastric mucosa [8].

A planar anterior and posterior view of about 10 min (140 keV, window 20%) is needed for the assessment of the pulmonary shunt. If a ^{99m}Tc-MAA SPECT is performed on the liver, this may be conveniently used to assess the absorbed doses on tumor areas and liver parenchyma. The basic assumption is that the therapeutic session will reproduce the exact catheter positioning with the injection of ^{90}Y-microspheres. Therefore ^{99m}Tc-MAA localization in the liver can be considered representative of ^{90}Y-microspheres biodistribution. Absorbed dose to lesions and to liver parenchyma can be determined by mathematically converting all liver voxel ^{99m}Tc-MAA SPECT uptake values to the absolute ^{90}Y activity and then converting these values to absorbed doses using the MIRD formalism [9].

2˙2. ^{90}*Y bremsstrahlung imaging.* – After therapeutic administration of ^{90}Y microspheres, a ^{90}Y bremsstrahlung SPECT scan can be performed to assess the localization of the microspheres in the treated area. Post-therapy imaging is required for two reasons: i) to assess possible migration of microspheres outside the liver region, thus warning clinicians of possible gastrointestinal complications (ulceration and bleeding in the gastrointestinal tract [10, 11]); ii) to determine absorbed dose to tumour and non-tumour tissue, being this figure an important predictor of treatment efficacy [12].

Secondary gamma (or bremsstrahlung) emission scans are possible due to the interaction of high-energy beta ^{90}Y particles with tissues. Unfortunately, the low photon yield, the septal penetration of high-energy photons and the continuous nature of the bremsstrahlung radiation represent a major drawback to the quantitative accuracy of ^{90}Y bremsstrahlung scintigraphy. In fact, approximately $23 \cdot 10^3$ bremsstrahlung photons with energy greater than 50 keV are emitted per MBq of ^{90}Y activity [13]. This requires a wide energy window to be set in order to maximize the gamma camera sensitivity. Figure 1 shows the poorer spatial resolution of bremsstrahlung imaging with respect to ^{99m}Tc-MAA SPECT imaging.

At present there still is no reference consensus on the acquisition parameters needed in clinical routine for optimal bremsstrahlung imaging and a number of approaches and gamma camera setups have been used. Kokabi *et al.* [14] performed bremsstrahlung acquisitions using 75 keV, 54% energy window, 30 stops at 40 seconds per stop for 60 projections. For images reconstruction OSEM algorithm was applied, 2 subsets, 30 iterations with attenuation correction. In another work Ahmadzadehfar and colleagues [15] for bremsstrahlung acquisitions used a medium-energy general purpose collimator with a very broad energy window of 55–250 keV to enhance the detection sensitivity of bremsstrahlung photons. Acquisition parameters for SPECT were a 128×128 matrix with

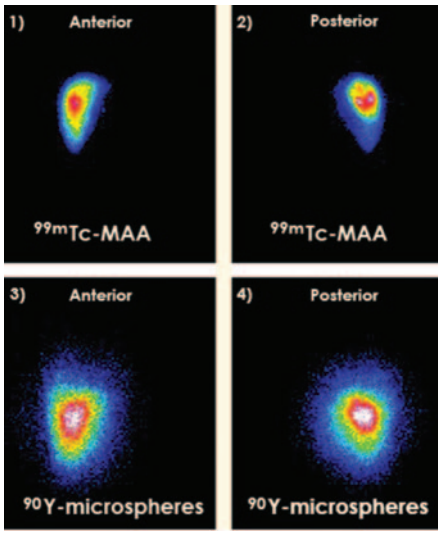

Fig. 1. – Comparison of ^{99m}Tc-MAA and ^{90}Y bremsstrahlung images of the same patient. Images 1 and 2 show scintigraphic ^{99m}Tc-MAA images in anterior and posterior projections respectively acquired 30 minutes after the administration of 185 MBq of ^{99m}Tc-MAA. Images 3 and 4 show the same patient acquired after the therapeutic administration of ^{90}Y-microspheres. It is evident that bremsstrahlung imaging suffers from a poorer spatial resolution due to scatter, septal penetration and continuous nature of energy spectrum.

64 frames (20 s per frame) and images were reconstructed using a Flash 3D algorithm with 8 iterations. Flamen [16] performed bremsstrahlung SPECT on a two-head gamma camera equipped with medium-energy all-purposes collimators. Two energy peaks centered around 70 keV (window 50%) and 192 keV (99% window) were recorded simultaneously. Imaging parameters were 32 projections, step and shoot over 180° with a 128 × 128 matrix. In a recent work Elshot [17] acquired bremsstrahlung photons in a 105–195 keV energy window using 120 projections over 360° and a 256 × 256 matrix, without post-reconstruction filtering. In another study Ulrich and colleagues [18] recorded images with a double-head gamma camera equipped with medium-energy general collimators. SPECT was performed with 128 projections over a 360° angle (30 s per projection) using a 128 × 128 matrix. The energy window was chosen in accordance with the suggestions by Minarik *et al.* [13] in the energy range of 75 keV (20% window width). Images were reconstructed by a 2-dimensional OSEM algorithm with 8 iterations and 4 subsets. Finally, a recent work by Ito and colleagues [19] dedicated to ^{90}Y bremsstrahlung SPECT using gamma cameras proposed three energy windows with the following widths: 50% (57–94 keV) centered at 75 keV, 30%(102–138 keV) at 120 keV, and 50% (139–232 keV) at 185 keV.

2˙3. ^{90}*Y PET imaging*. – It is known that ^{90}Y has a minor branch to the 0^+ first excited state of ^{90}Zr at 1.76 MeV, that is followed by a β^+/β^- emission. This internal pair production has been largely studied in the past because it is generated by a rare electric monopole transition ($E0$) between the states $0^+/0^-$ of ^{90}Zr. A thorough explanation of the emission of β^+ particles via internal pair production in the $0^+/0^-$ transition of ^{90}Zr is provided elsewhere [20] and will not be repeated here.

For decades, this internal pair production was not exploited in nuclear medicine. However in recent years, despite the branching ratio for pair-production being very small, $(3.186 \pm 0.047) \cdot 10^{-5}$, the positronic emission has been successfully used for PET acquisitions of ^{90}Y-labelled radiopharmaceuticals. A number of phantom and patient studies have been conducted by our group on this topic [21-23].

In particular, PET imaging of ^{90}Y microspheres presents two major advantages: i) direct visualization of the real therapeutic agent after administration; ii) the possibility of obtaining high-resolution images for retrospective dosimetry. At present it is generally acknowledged that ^{90}Y PET/CT is superior to ^{90}Y bremsstrahlung SPECT/CT for the assessment of target and non-target activity.

The quality of images obtained via PET imaging of ^{90}Y internal pair production is limited by the very small β^+ branching fraction and therefore necessitates longer acquisition times (in the range 20 to 40 minutes) than traditional β^+ emitting radionuclides. As an example, ^{18}F emits 967 β^+ per 1000 decays. Furthermore, the accuracy of quantitative ^{90}Y PET imaging is strongly related to the knowledge of the internal pair production branching ratio. Therefore it is desirable that in the future accurate measurements of the β^+ emission probability will be performed in order to validate the intensity of the branching ratio and possibly reduce the related standard uncertainty (currently about 1.5% [24]).

Of note, a recent multicenter comparison of quantitative ^{90}Y PET for dosimetric evaluation after radioembolization with resin microspheres (QUEST phantom study, [25]) showed that Time-of-Flight (ToF) PET/CT scanners are capable of achieving higher accuracy in quantitative ^{90}Y imaging. In the QUEST phantom study the quantitative accuracy of ^{90}Y imaging across 69 ToF and non-ToF PET/CT scanners (37 with ToF mode) was scrutinized, for a total of 47 international sites involved.

It should be noted that today's ToF PET scanners are generally equipped with lutitium-based crystals (*e.g.*, cerium-doped LYSO or cerium-doped LSO) due to its superior timing resolution. The major drawback with these scintillators is the presence of the naturally occurring isotope ^{176}Lu, which gives rise to background count rates within the crystal. As a consequence, a scenario of low counts and high random fraction, as in ^{90}Y PET/CT imaging, may hinder accurate quantification. An extensive overview of the degrading factors affecting ^{90}Y PET/CT quantitative imaging can be found in [26].

3. – Dosimetry following ^{90}Y PET imaging: A phantom study

A phantom study aimed to benchmark different dosimetric approaches was jointly performed by Santa Maria Goretti Hospital (Latina, Italy) and the National Institute of Ionizing Radiation Metrology (INMRI - Rome, Italy). An anthropomorphic phantom provided with a cylindrical insert (mimicking an hepatic lesion), a liver cavity and a background compartment was used to perform ^{90}Y PET acquisitions [27]. ^{90}Y PET images were acquired with a non-ToF GE Discovery ST PET/CT scanner, voxel size $2.73 \times 2.73 \times 3.27\,\mathrm{mm}^3$.

Measurements were performed using a 6:1 tumor to liver activity concentration ratio. The first scan was performed with an activity concentration of 5498 kBq mL^{-1} for the lesion insert and 887 kBq mL^{-1} for the liver. The anthropomorphic phantom was then acquired at days 4, 5, 6 and 12 down to an activity concentration of 312.9 kBq mL^{-1} for the lesion insert and 50 kBq mL^{-1} for the liver. The background compartment of the phantom was filled with non-radioactive water. Scan time was 15 minutes for acquisitions at day 1 and 4, and 30 minutes for acquisitions at day 5, 6 and 12 (fig. 2).

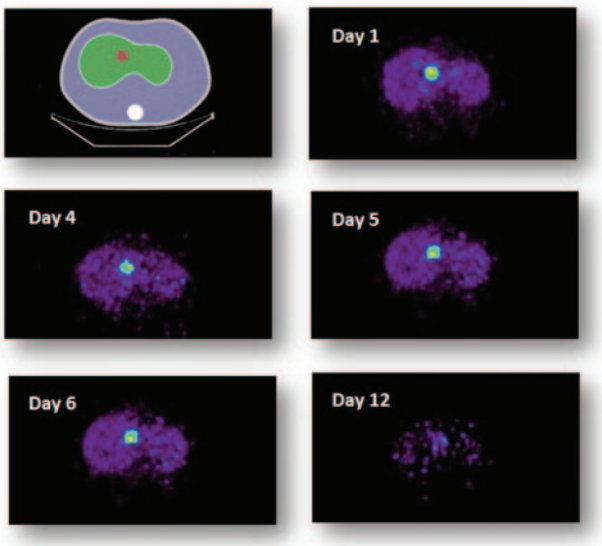

Fig. 2. – Acquisitions in anthropomorphic geometry. (a) Anthropomorphic phantom used for ^{90}Y-PET acquisitions. The phantom is provided with a cylindrical insert simulating an hepatic lesion (19.13 mL, diameter 28.5 mm, height 30 mm) fixed into the liver compartment (b)–(f) ^{90}Y-PET acquisitions performed at days 1, 4, 5, 6, 12, respectively.

Absorbed doses to the cylindrical insert (lesion) were calculated benchmarking different computational algorithms including: i) full Monte Carlo (MC) using RAYDOSE; ii) Dose-Volume-Kernel convolution using Philips STRATOS; iii) local deposition (LD); iv) MC N-Particle code (MCNP4c), assuming uniform activity distribution within the insert; v) MIRD analytical approach. A brief description of each of the dose algorithms is given below for ease of reference. For more in-depth description of the dose computational approaches see [27].

3˙1. *Full Monte Carlo dose calculation using RAYDOSE.* – RAYDOSE is a Geant4-based applicationcapable of generatig patient-specific 3D dose maps for molecular radiotherapy on the basis of imaging studies. CT DICOM images are used to model patient geometry, while PET scans are employed to assess radionuclide kinetics and distribution at the voxel level. RAYDOSE has been validated against reference data and experimental measurements. The reader is referred to [28] for a detailed description of the code. In the present study, RAYDOSE was used to assess the absorbed dose to the cylindrical insert using ^{90}Y-PET of the anthropomorphic phantom.

3˙2. *Dose-Volume-Kernel convolution.* – Dose calculation using the Dose-Volume-Kernel approach was performed using the software STRATOS, part of the IMALYTICS Research Workstation (Philips). ^{90}Y-PET activity data were co-registered with CT scans of the anthropomorphic phantom and the time-integrated activity at the voxel level was calculated. The cumulated activity at the voxel level is then convolved with pre-loaded voxel S factors to obtain the absorbed dose distribution in the cylindrical insert. Figure 3 shows the convolution kernel for ^{90}Y as calculated from MCNP4c simulations.

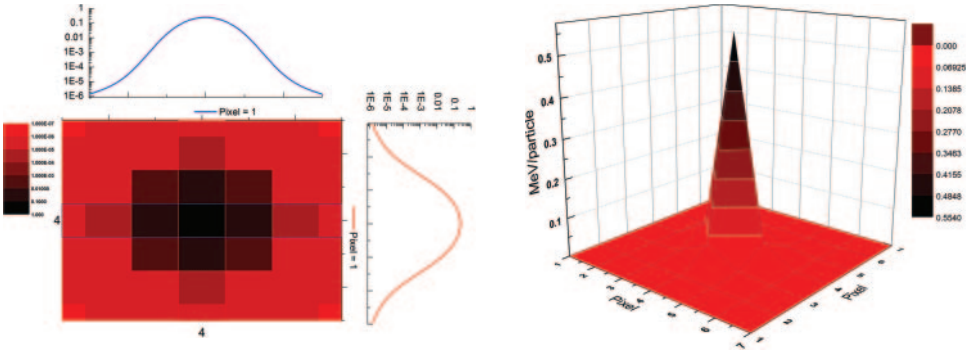

Fig. 3. – Convolution kernel $K(x, y, z)$ for ^{90}Y as calculated from MCNP4c simulations. (Left) normalized convolution kernel on the transverse (x, y) plan (maximum dose deposition=1). (Right) absolute 3D convolution kernel (MeV) per pixel.

3˙3. *Local deposition.* – Due to its simplicity of implementation, the local deposition algorithm has recently gained popularity as an alternative means to estimate the absorbed dose at the voxel level. The local deposition algorithm is based on the assumption that the energy released from each decay of ^{90}Y is entirely deposited in the voxel where the decay occurred. Under the aforementioned assumption, the absorbed dose D_{voxel} within a voxel (assumed to be composed of water) can be calculated as follows:

$$D_{voxel}(Gy) = \frac{C_0(\mathrm{Bq/mL}) \cdot 4.998 \cdot 10^{-8}(\mathrm{J \cdot s})}{\rho_{water}(\mathrm{kg/mL})}. \tag{1}$$

3˙4. *MC N-Particle (MCNP) code.* – MCNP is a general-purpose Monte Carlo N-Particle code that can be used for (coupled) neutron, photon, electron transport. The code is widely used in medical physics applications. In the present study MCNP version 4c was used to asses the absorbed dose to the cylindrical insert in the liver compartment considering a uniform distribution of ^{90}Y into the cylinder. The absorbed dose was calculated using the *f8 tally, *i.e.* determining the net energy (MeV) deposited in a scoring region from the coupled photonelectron transport.

3˙5. *MIRD analytical approach.* – The MIRD Schema for ^{90}Y-microspheres is described in [29]. On a macroscopic scale, the average absorbed dose, D_{avg}, to a given volume of interest of mass m (m_{insert} in the present case) can be derived using eq. (2)

$$D_{avg}(Gy) = \frac{A_0(\mathrm{GBq}) \cdot 49.98(\mathrm{J \cdot s})}{m_{insert}(\mathrm{kg})}, \tag{2}$$

where A_0 is the initial ^{90}Y activity and the factor 49.98 (often rounded off to 50) is the cumulative energy deposited in tissue (water) by ^{90}Y.

4. – Results and discussions

Recent research indicates that ^{90}Y-PET images are inherently noisy due to the extremely small positron emission branching fraction of ^{90}Y, which results in low

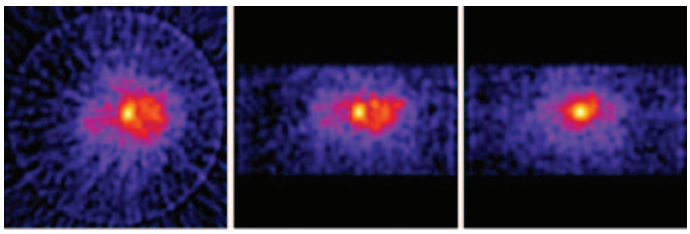

Fig. 4. – Bremsstrahlung SPECT image of the anthropomorphic phantom. Acquisition performed at day 8 using a GE Infinia SPECT system. Voxel size, $4.41 \times 4.41 \times 4.41\,\mathrm{mm}^3$, energy window lower/upper limit 63/77 keV, total scan time 50 minutes.

true-coincidence count rate. This finding was confirmed in the present study. Despite the cylindrical insert being uniformly filled with ^{90}Y, visual inspection of the images showed the presence of hot and cold spots, *i.e.* heterogeneous activity distributions (fig. 2). However, our data confirm that^{90}Y-PET is superior to ^{90}Y bremsstrahlung SPECT for the assessment of target activity, provided that enough counts are registered by the PET scanner. Figure 4 shows a bremsstrahlung image of the anthropomorphic phantom acquired at day 8, using a GE Infinia SPECT system. The hot insert results significantly blurred and the liver compartment is barely discernible.

As a general rule, all dose algorithms provided comparable dose estimates. Figure 5 shows a comparison of absorbed doses calculated in the cylindrical insert using different computational approaches. Results are presented in terms of average dose over the 5 data points (corresponding to acquisitions at days 1,4,5,6 and 12, coloured boxes),

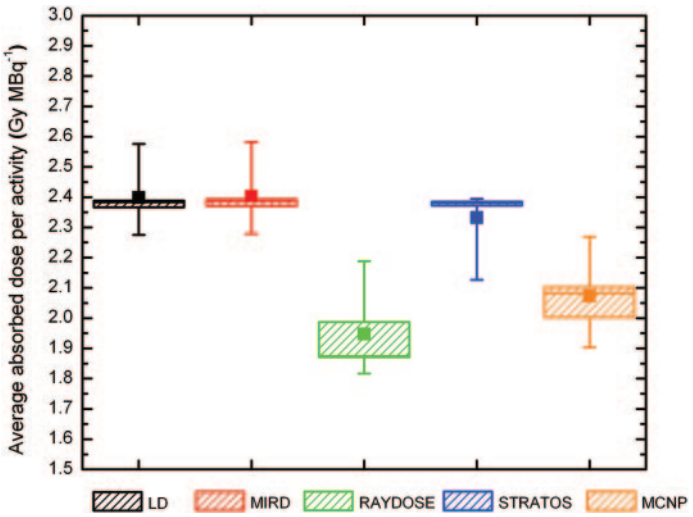

Fig. 5. – Comparison of absorbed doses per unit activity (Gy/MBq) of ^{90}Y in the cylindrical sample. For each computational algorithm, results are presented in terms of: average dose over the 5 data points (corresponding to acquisitions at days 1,4,5,6 and 12, coloured boxes), minimum and maximum dose (indicated with (-) symbol) and 25th and 75th percentile (represented with diagonal line pattern)

minimum and maximum dose (indicated with (-) symbol) and 25th and 75th percentile (represented with diagonal line pattern). Absorbed doses are reported per unit of ^{90}Y activity (Gy/MBq) in the sample.

Local deposition, MIRD analytical algorithm and STRATOS provided results in close agreement (within 3%). Similarly, both MC codes (RAYDOSE and MCNP) returned comparable average dose values, with an agreement within 6%. Of note, dose values obtained with LD, analytical algorithm and STRATOS systematically overestimate MC calculations. It is likely that the foremost cause of this minor discrepancy is the presence of the PMMA wall of the cylindrical insert, that was considered only in Raydose and MCNP simulations.

A maximum deviation of about 19% was obtained between the MIRD analytical algorithm and RAYDOSE. It is worth pointing out that D'Arienzo and colleagues [27] have found an excellent agreement (within 3%) between absorbed dose assessed with RAYDOSE and doses measured using LiF:Mg,Cu,P thermoluminescence dosimeters, in the same geometry. This finding confirms that direct Monte Carlo radiation transport can be regarded as the most accurate of all currently available dose estimation algorithms.

The present data suggest that due to the negligible computational burden LD algorithm may be regarded as a plausible candidate for routine dosimetry using ^{90}Y-PET images. In fact, the local deposition algorithm is essentially a rescaling of the voxel activity value and is therefore very fast. LD has the potential to provide accurate dose estimates whenever the energy released by charged particles can be assumed to be locally absorbed within the same voxel as the decay. The other assumption of local deposition algorithm is that the full width at half maximum (FWHM) of the point spread function (PSF) should be larger than the dose point kernel. This is because the output images can be regarded as a convolution of the real object with the PSF of the system. In the ideal case where PSF = Kernel, the imaging system simulates the energy transport among voxels and the output image can be regarded as the absorbed dose map.

It is worth pointing out that our experiments are consistent with previous results. Previous research by Pasciak and Erwin [30] attempted to quantify the effectiveness of several sophisticated patient-specific dose algorithms to perform voxelized dosimetric computations. The authors proved that the local deposition method generates dose estimates comparable with (and in some cases more accurate than) 3-D MC transport, with a negligible computational burden. In another study the same author [31] suggested the LD method for routine post-radioembolization ^{90}Y dosimetry based on PET/CT imaging. Along these lines, other authors have proved that the LD method represents a viable alternative to traditional algorithms [32, 33].

Further experimental investigations are needed to assess to what extent this approach can be extended to other geometries and different voxel sizes.

5. – Conclusions

Returning to the question posed in the title, we have obtained comprehensive results proving that all dose algorithms performed satisfactorily, with maximum deviations below 19%, for the experimental conditions considered. As a general rule, direct Monte Carlo radiation transport can be regarded as the most accurate of all currently available dose estimation algorithms. However, due to its immediate use and ease of implementation, the LD algorithm has the potential to provide reliable dose estimates in a clinical setting where resource-intensive computational systems are not always available.

* * *

The research leading to these results has received funding from the European Commission (EC), Grant Agreement N 217257 between the EC and EURAMET under the Seventh Framework Programme. I would like to give very special thanks to the following colleagues: Maria Pimpinella, Marco Capogni, Vanessa De Coste, Luca Filippi, Emiliano Spezi, Nick Patterson, Francesca Mariotti, Paolo Ferrari, Paola Chiaramida, Michael Tapner, Alexander Fischer, Timo Paulus, Roberto Pani, Giuseppe Iaccarino, Marco D'Andrea, Lidia Strigari and Oreste Bagni. I could not have accomplished this results without their help and support.

REFERENCES

[1] Stubbs R. and Wickremesekera S., *HPB*, **13** (2004) 3.
[2] Ho S., Lau W. Y., Leung T. W., Chan M., Ngar Y. K., Johnson P. J. and Li A. K., *Eur. J. Nucl. Med.*, **23** (1996) 8.
[3] Lau W. Y., Ho S., Leung T. W., Chan M., Ho R., Johnson P. J. and Li A. K., *Int. J. Radiat. Oncol. Biol. Phys.*, **40** (1998) 3.
[4] Ahmadzadehfar H., *J. Nucl. Med.*, **51** (2010) 8.
[5] Talanow R., Levitin A., Kikano R., Shrikanthan S. and Srinivas S., *RSNA Annual Meeting* (2010).
[6] Wondergem M., Smits M. L., Elschot M., de Jong H. W., Verkooijen H. M., van den Bosch M. A., Nijsen J. F. and Lam M. G., *J. Nucl. Med.*, **54** (2013) 8.
[7] Kennedy A. *et al.*, *Int. J. Radiat. Oncol. Biol. Phys.*, **68** (2007) 1.
[8] Vouche M. *et al.*, *J. Nucl. Med. Radiat. Ther.*, **2** (2011) 113.
[9] Gulec S. A., Mesoloras G. and Stabin M., *J. Nucl. Med.*, **47** (2006) 7.
[10] Murthy R. *et al.*, *J. Vasc. Interv. Radiol.*, **18** (2007) 4.
[11] Riaz A. *et al.*, *J. Vasc. Interv. Radiol.*, **20** (2009) 9.
[12] Chiesa C. *et al.*, *Q J. Nucl. Med. Mol. Imaging*, **55** (2011) 2.
[13] Minarik D., Sjogreen G. K. and Ljungberg M., *Phys. Med. Biol.*, **53** (2008) 2.
[14] Kokabi N., Galt J. R. and Xing M., *J. Vasc. Interv. Radiol.*, **25** (2014) 2.
[15] Ahmadzadehfar H. *et al.*, *Eur. J. Nucl. Med. Mol. Imaging*, **38** (2011) 7.
[16] Flamen P., Vanderlinden B. and Delatte P., *Phys. Med. Biol.*, **53** (2008) 22.
[17] Elschot M., Vermolen B. J. and Lam M. G., *PLoS One*, **8** (2013) 2.
[18] Ulrich G. *et al.*, *J. Vasc. Interv. Radiol.*, **54** (2013) 4.
[19] Ito S. *et al.*, *Ann. Nucl. Med.*, **23** (2009) 3.
[20] D'Arienzo M., *Atoms*, **1** (2013) 1.
[21] Bagni O. *et al.*, *Nucl. Med. Commun.*, **33** (2012) 2.
[22] D'Arienzo M. *et al.*, *Nucl. Med. Commun.*, **33** (2012) 6.
[23] D'Arienzo M. *et al.*, *Ann. Nucl. Med.*, **27** (2013) 7.
[24] Selwyn R. G., *Appl. Radiat. Isot.*, **65** (2007) 3.
[25] Willowson K. P., Tapner M., QUEST Investigator Team and Bailey D.L., *Eur. J. Nucl. Med. Mol. Imaging*, **42** (2015) 8.
[26] D'Arienzo M., *Quantitative postradioembolization imaging using PET/CT*, in *Handbook of Radioembolization: Physics, Biology, Nuclear Medicine, and Imaging*, edited by Pasciak S., Bradley Y. and McKinney J. M. (CRC Press, Boca Raton, USA) 2016, pp. 229–249.
[27] D'Arienzo M., *Eur. J. Nucl. Med. Mol. Imaging*, **43(Suppl. 1)** (2016) 1.
[28] Marcatili M., Pettinato C., Daniels S., Lewis G., Edwards P., Fanti S. and Spezi E., *Phys. Med. Biol.*, **58** (2013) 8.
[29] Gulec S. A., Mesoloras G. and Stabin M., *J. Nucl. Med.*, **47** (2006) 7.
[30] Pasciak A. S. and Erwin W. D., *IEEE Trans. Med. Imaging*, **28** (2009) 11.
[31] Pasciak A. S., Bourgeois A. C. and Bradley Y. C., *Front. Oncol.*, **4** (2014) 121.
[32] Traino A. C. *et al.*, *Med. Phys.*, **40** (2013) 4.
[33] Ljungberg M. and Sjgreen-Gleisner K., *Acta Oncol.*, **50** (2011) 6.